

---

Mechanical Engineering Faculty Publications

Mechanical Engineering Department

---

4-2018

## Optimal Mixed Tracking/Impedance Control With Application to Transfemoral Prostheses With Energy Regeneration

Gholamreza Khademi  
*Cleveland State University*

Hanieh Mohammadi  
*Cleveland State University*

Hanz Richter  
*Cleveland State University, h.richter@csuohio.edu*

Daniel J. Simon  
*Cleveland State University, d.j.simon@csuohio.edu*

Follow this and additional works at: [https://engagedscholarship.csuohio.edu/enme\\_facpub](https://engagedscholarship.csuohio.edu/enme_facpub)

 Part of the [Biomechanical Engineering Commons](#)

[How does access to this work benefit you? Let us know!](#)

---

### Recommended Citation

Khademi, Gholamreza; Mohammadi, Hanieh; Richter, Hanz; and Simon, Daniel J., "Optimal Mixed Tracking/Impedance Control With Application to Transfemoral Prostheses With Energy Regeneration" (2018). *Mechanical Engineering Faculty Publications*. 371.  
[https://engagedscholarship.csuohio.edu/enme\\_facpub/371](https://engagedscholarship.csuohio.edu/enme_facpub/371)

This Article is brought to you for free and open access by the Mechanical Engineering Department at EngagedScholarship@CSU. It has been accepted for inclusion in Mechanical Engineering Faculty Publications by an authorized administrator of EngagedScholarship@CSU. For more information, please contact [library.es@csuohio.edu](mailto:library.es@csuohio.edu).

# Optimal Mixed Tracking/Impedance Control With Application to Transfemoral Prostheses With Energy Regeneration

Gholamreza Khademi , Hanieh Mohammadi, Hanz Richter, and Dan Simon

biomedical devices, robotic manipulators, spacecraft, industrial systems and prosthetics. For instance, industrial robots with energy recovery can provide significant economic benefits [1]. Transfer of energy to a storage element or an external source during operation is the key purpose of energy regeneration. Various storage media can be used depending on the application. For instance, reservoirs and accumulators might be used in hydraulic and pneumatic domains, while ultracapacitors are typically used in electrical domains. The main characteristics of ultracapacitors are fast charge and discharge rates, which has made them widely used in spacecraft [2], road vehicles [3], and robots [4]–[6].

Control and energy regeneration for prosthetic legs have received considerable attention over the past few decades [7]–[11]. The pioneering research in this area was conducted in 1980 [12]–[14] where capacitors were used as the storage element, but the required capacitances were not available at that time. Energy regeneration for prostheses with electrical storage elements was investigated in [15]. Energy regeneration for hydraulic prostheses was investigated in [16]–[18]. A minimization problem was solved to conserve energy in a manipulator in [19] and [20], where the authors attempted to save energy by minimizing the dissipation losses and viewed the problem as an optimal path planning problem, but did not consider the influence of external forces on energy regeneration.

The energy profile of healthy subjects during normal walking shows that the knee joint provides a net surplus energy, while the ankle requires net energy consumption [21]. The knee joint motion includes an extended time of negative power, whereas the ankle motion does not include considerable negative power during gait. In fact, the time periods of negative power at the knee are the same as the periods of positive power at the ankle. There is thus natural energy transfer through tendons and ligaments from the knee to the ankle during these periods. This motivates the idea of energy capture from the knee to alleviate the power requirement at the ankle, or at the knee during later time periods. In this study, we mimic the biological transfer of energy using ultracapacitors instead of ligaments and tendons.

This idea has also motivated other researchers to develop prosthetic legs with energy regeneration. For example, researchers in [22] developed a passive prosthetic leg that transfers knee energy surplus to the ankle. In recent work [23], [24] a generalized framework for robotic modeling and control with energy regeneration was proposed, where a

## I. INTRODUCTION

**M**OTION control systems with energy regeneration have advanced rapidly in recent years. Applications include

general robotic configuration with rigid links was considered and energy regeneration was taken into account. Inverse dynamic control was used to control the manipulator. To improve control and compensate for model uncertainties, robust passivity-based control was suggested in [24]. The control design was implemented and experimentally tested on a PUMA robot where the feasibility of energy regeneration at the semi-active joints was demonstrated. Semi-active virtual control was used to meet a given control objective. The virtual control was implemented by adjusting certain parameters of the semi-active joints. However, the influence of external forces on energy regeneration in powered prostheses was not considered.

The contribution of this paper is a discussion of the effect of external forces on energy regeneration, the consideration of this effect in a multi-objective optimization problem, and the use of cubic splines for time-varying impedance. We model a robotic manipulator with energy regenerative electronics, where the manipulator has both actively and semi-actively controlled joints. We consider the effect of external forces using an energy balance equation. For instance, ground reaction force plays the role of external forces in the prosthetic leg application. We investigate the influence of ground reaction force and show that it can greatly affect energy regeneration. We therefore design optimal passivity-based tracking/impedance control for the robotic manipulator to indirectly control external force. Deviations from the reference trajectories result from the impedance controller, which enforces a desired relationship between external force and deviation from the reference trajectories. This paper shows that greater deviations from the reference trajectories provide better energy regeneration, and better tracking of reference trajectories result in less energy regeneration. That is, trajectory tracking and energy regeneration are conflicting objectives. We thus use MOO to find optimal impedance control parameters to compromise between the two objectives. Constrained non-dominated sorting biogeography-based optimization (NSBBO) is the algorithm that we use for this purpose. We have chosen to use BBO in this paper because it has demonstrated competitive performance relative to other state-of-the-art evolutionary algorithms [25]. We have chosen to use nondominated sorting because it has demonstrated competitive performance in terms of finding optimal Pareto fronts relative to other state-of-the-art MOO algorithms [26]. MOO results in a set of non-dominated solutions called a Pareto front, and we use a pseudo-weight approach to select from among the Pareto front solutions.

To demonstrate our results, we use a three degree of freedom test robot that mimics able-bodied walking. We solve the MOO problem to obtain optimal constant impedance parameters for the controller. We show that a tradeoff solution results in fair tracking and positive energy regeneration with slight chatter in the semi-active knee joint. To improve the results and remove chattering, another MOO problem with time-varying impedance is solved. Normalized hypervolume and relative coverage are used to show that the Pareto front with time-varying impedance provides better solutions than the Pareto front with constant impedance.

Our results support the possibility of net energy regeneration at the semi-active joint with acceptable tracking error. The results indicate that ultracapacitor systems with advanced

controls and optimization have the potential to significantly reduce external power requirements in a powered prosthesis.

This paper builds upon and improves on previous work [27] by incorporating a more complete and comprehensive discussion of the model, the controller, the optimization problem, and the simulation and experimental results.

The rest of the paper is outlined as follows. Section II reviews mathematical modeling, manipulator dynamics, the joint mechanism structure, and the energy storage element. Section III derives the mixed tracking/impedance controller. Section IV investigates the effect of external force on energy regeneration. Section V defines the tradeoff between the control objectives as a multi-objective optimization problem. Section VI discusses the test robot hardware, the prosthesis, and the test setup. Section VII presents simulation results, experimental results, and potential improvements and limitations. Section VIII discusses conclusions.

## II. MATHEMATICAL MODELING

Here we present the configuration of a general robotic manipulator with energy regenerative electronics [24]. The robotic manipulator has  $n$  degrees-of-freedom (DOF) consisting of a serial kinematic chain of rigid links connected by joints. The first  $n - m$  joints are fully active, while the remaining  $m$  joints are semi-active. The energy of a fully active joint is provided by external power, while the energy of a semi-active joint is obtained from an on-board storage element with a regenerative system.

### A. Manipulator Dynamics

The motion of an  $n$ -DOF robotic manipulator is described by the following standard nonlinear equation:

$$D(q)\ddot{q} + C^o(q, \dot{q})\dot{q} + \mathcal{R}^o(\dot{q}) + g^o(q) + T_e = \tau \quad (1)$$

where  $q$  is the  $n \times 1$  vector of joint displacements.  $D(q)$ ,  $C^o(q, \dot{q})$ ,  $\mathcal{R}^o(\dot{q})$ , and  $g^o(q)$  are the inertia matrix, Coriolis matrix, nonlinear friction term, and the gravity vector, respectively.  $\tau$  is the vector of joint control forces or moments applied by the joint mechanisms (JMs), which are actuators that deliver the required force and torque to prismatic and rotary joints.  $T_e$  is a vector that accounts for the combined effect of external forces or moments applied to each joint of the manipulator, and is given by

$$T_e = \sum_{i=1}^{n_f} (J^i)^T F_{ei} \quad (2)$$

where  $F_{ei}^T = [f_{ix} \ f_{iy} \ f_{iz} \ M_{ix} \ M_{iy} \ M_{iz}]$  is the external force and moment applied at point  $i$  on the manipulator in Cartesian space, and  $J^i$  indicates the kinematic Jacobian at point  $i$ . Semi-active joints in (1) will be augmented with the JM models in Section II-C.

### B. Semi-Active Joints With Regenerative Electronics

In this section, we discuss the configuration of energy regenerative electronics for semi-active joints of a robotic manipulator. In semi-active joints, the JM only *exchanges* mechanical

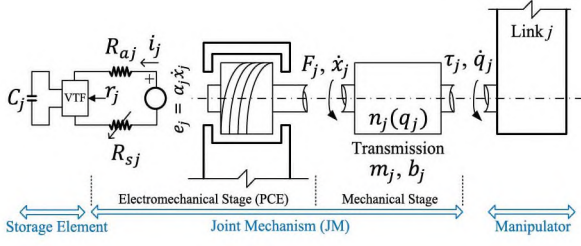


Fig. 1. Configuration of an energy-storing element and a joint mechanism (JM) system in a semi-active joint, where JM has a pure mechanical stage and an electromechanical power conversion element (PCE).

power with the robot. Each JM has a purely mechanical stage and a power conversion element (PCE). The pure mechanical stage is composed of transmission, inertia, and friction, with its output connected to a semi-active robotic link with port variables  $\tau_j$  and  $\dot{q}_j$ . The input of the mechanical stage of the JM with port variables  $F_j$  and  $\dot{x}_j$  is connected to a PCE such as a DC electric motor/generator. The PCE is a two-port element that transforms energy between two domains to regulate power transmission. The PCE is connected to an external power source in a fully actuated JM, and it is connected to a compatible storage device in a semi-actuated JM. In this paper, an ultracapacitor is considered as the energy-storing element. An ultracapacitor has a fast charge and discharge rate, which makes it an ideal choice for robotic energy regeneration.  $Ce = \int f dt$  is the linear constitutive law for the ultracapacitor, where  $C$  is the electric capacitance,  $e$  and  $f$  are the voltage and current, and  $y = \int f dt$  is the charge of the ultracapacitor.

An ideal variable transformer (VTF) is placed between the ultracapacitor and the DC machine to control the energy flow to and from the ultracapacitor through adjustable parameter  $r_j$ . Since  $r_j$  can be adjusted to be negative or positive, a four-quadrant (4Q) VTF is required [28]. An off-the-shelf 4Q servo amplifier realizes the VTF. Fig. 1 illustrates the configuration of a semi-active joint with energy regenerative electronics.

In Fig. 1,  $n_j(q_j)$  is the gear ratio function and  $m_j$  and  $b_j$  are the moment of inertia and viscous damping of the gear transmission and motor reflected to the input of the transmission.  $\alpha_j$  and  $R_{a_j}$  are the torque constant and motor armature resistance, respectively. To control the energy storage rate in the ultracapacitor, an additional series resistance  $R_{s_j}$  is added, whose power dissipation is controlled by a VTF through adjustable parameter  $s_j$ .

A semi-active JM can always operate properly as long as the capacitor is charged. If the capacitor completely discharges, a backup power supply would power the JM in active mode while the capacitor would be bypassed until it recharges. If the capacitor completely charges and the energy storage rate is positive, the ultracapacitor could be damaged. In this case,  $s_j$  is used in an outer supervisory control loop to connect a series resistance to reduce the energy storage rate until the capacitor voltage falls below an upper limit [24]. Note that  $\tau_j \dot{q}_j < 0$  indicates that mechanical energy is transferred to the JM from the robotic link, indicating regeneration mode, while  $\tau_j \dot{q}_j > 0$  indicates an opposite flow of energy, indicating driving mode.

### C. Augmented Robot Dynamics

In general, JMs can be considered for both active and semi-active joints. Recall that a joint might be active, in which case it does not include energy storage; or it might be semi-active, in which case it does include energy storage. Also, a joint might include a JM, in which case it includes actuator dynamics; or it might not include a JM, in which case it does not include actuator dynamics and torque or force is controlled directly. To simplify the augmented model in this paper, JMs are used only for semi-active joints.

For the semi-active joints, we obtain the control signal  $\tau_j$  of the manipulator dynamics in terms of  $F_j$  with the help of a bond graph [29]. Modeling the DC machine as an ideal gyrator leads to the formulation of  $F_j$  in terms of ultracapacitor voltage  $y_j/C_j$ , where  $y_j$  is the electric charge. We find a relationship between the control signal  $\tau_j$  and the ultracapacitor voltage, and then we substitute the result in the manipulator dynamics of (1) to form the following augmented dynamics:

$$M(q)\ddot{q} + C(q, \dot{q})\dot{q} + \mathcal{R} + g + T_e = u \quad (3)$$

where  $u_j = \tau_j$  is actively controlled for  $j \in A = \{1, 2, \dots, n-m\}$ , and  $u_j = \frac{\alpha_j \tau_j}{C_j R_j} y_j$  is semi-actively controlled for  $j \in S = \{n-m+1, n-m+2, \dots, n\}$ , where  $A$  and  $S$  indicate active and semi-active joints. The mass matrix  $M$ , Coriolis matrix  $C$ , and friction term  $\mathcal{R}$  for the augmented manipulator dynamics are given as follows:

$$M_{ij} = \begin{cases} D_{ij} & \text{for } (i \neq j \text{ and } j \in S) \text{ or } j \in A \\ D_{jj} + m_j n_j^2(q_j) & \text{for } (i = j \text{ and } j \in S) \end{cases}$$

$$C_{ij} = \begin{cases} C_{ij}^o & \text{for } (i \neq j \text{ and } j \in S) \\ & \text{or } j \in A \\ C_{ij}^o + m_j n_j(q_j) \frac{dn_j(q_j)}{dq_j} \dot{q}_j & \text{for } (i = j \text{ and } j \in S) \end{cases}$$

$$\mathcal{R}_j = \begin{cases} \mathcal{R}_j^o & \text{for } j \in A \\ \mathcal{R}_j^o + \left( b_j n_j^2(q_j) \dot{q}_j + \frac{a_j^2}{R_j} \right) \dot{q}_j & \text{for } j \in S \end{cases} \quad (4)$$

where  $a_j = \alpha_j n_j(q_j)$  and  $R_j = R_{a_j} + s_j^2 R_{s_j}$ . Note that the gravity vector does not change:  $g = g^o$ . The basic characteristics of skew-symmetry and passivity are still maintained for the augmented robot dynamics [23]. To simplify the control design, the back-emf term  $a_j^2 \dot{q}_j / R_j$  in the augmented friction vector  $\mathcal{R}_j$  of (4) is canceled, so the control law  $u$  has the form

$$u_j = \begin{cases} v_{c_j} & \text{for } j \in A \\ v_{c_j} + \frac{a_j^2}{R_j} \dot{q}_j & \text{for } j \in S \end{cases} \quad (5)$$

where  $v_c$  is the desired virtual control. In case we lack prior knowledge of the JM parameters, we can use either robust or adaptive control approaches to cancel the back-emf term [30]. In Section III we design  $v_c$  for the augmented dynamics to achieve the control objectives. The control law  $u_j$  is then obtainable using (5). For  $j \in A$ , the control law  $u_j = \tau_j$  is directly commanded, while for  $j \in S$  the control law is provided by the storage element and is in the form  $u_j = \frac{\alpha_j \tau_j}{C_j R_j} y_j$ . Note that  $s_j$

is set to be constant, assuming that the ultracapacitor voltage is less than the upper threshold, so  $r_j$  is the only adjustable parameter:

$$r_j = \frac{u_j R_j}{a_j \frac{y_j}{C_j}} \quad (6)$$

### III. VIRTUAL CONTROL DESIGN

In this section, we use passivity-based (PB) control [31] to design a virtual control  $v_e$  for the augmented robot dynamics of (3) without the back-emf term. The control objective is to track desired motion references for all robotic joints. A subset of the joints must have pure motion tracking, while the remaining joints are controlled to achieve a trade-off between tracking accuracy and energy regeneration by specification of a target impedance. The first subset of joints is referred to as motion-controlled (MC), while the second as impedance-controlled (IC). In the prosthesis application, MC joints represent residual healthy joints in an amputee, while IC joints correspond to powered prosthetic devices with energy regeneration.

A target impedance is imposed to regulate the response of the tracking errors to external forces (and consequently to control stored energy). The first  $n - m$  joints (active) are MC, while the remaining  $m$  joints (semi-active) are IC.

We partition the joint displacement as  $q^T = [q_{MC}^T \ q_{IC}^T]$ , and  $T_e^T = [T_{MC}^T \ T_{IC}^T]$ , where  $q^d(t)$  is the desired motion trajectory in joint space. Tracking error is defined as  $\tilde{q} = q - q^d$ . The target impedance is specified as

$$I\dot{\tilde{q}}_{IC} + b\ddot{\tilde{q}}_{IC} + k\tilde{q}_{IC} = -T_{IC} \quad (7)$$

where  $I$ ,  $b$ , and  $k$  are diagonal matrices that represent the desired inertia, damping, and stiffness, respectively. Note that  $F_e = 0$  implies that asymptotic tracking can be achieved for IC joints. To achieve the target impedance, the variable structure method for robust control (VSMRC) [32] is used:

$$\dot{z} = Az + k_p \tilde{q}_{IC} + k_d \dot{\tilde{q}}_{IC} + k_f T_{IC} \quad (8)$$

where  $z$  is the  $m \times 1$  compensator.  $A$  is a negative semi-definite matrix, and  $k_p$ ,  $k_d$ , and  $k_f$  are chosen to achieve the target impedance. Using previous results on PB control [31], [33], the desired virtual control is chosen as

$$v_e = M(q)a + C(q, \dot{q})v + \mathcal{R}(\dot{q}) + g(q) - Kr + T_e \quad (9)$$

where  $a$ ,  $v$  and  $r$  are partitioned as  $a^T = [a_{MC}^T \ a_{IC}^T]$ ,  $v^T = [v_{MC}^T \ v_{IC}^T]$ , and  $r^T = [r_{MC}^T \ r_{IC}^T]$ , and

$$v_{MC} = \dot{q}_{MC}^d - \Lambda_{MC} \tilde{q}_{MC} \quad (10)$$

$$a_{MC} = \dot{v}_{MC} = \dot{q}_{MC}^d - \Lambda_{MC} \dot{\tilde{q}}_{MC} \quad (11)$$

$$r_{MC} = \dot{q}_{MC} - v_{MC} = \dot{q}_{MC}^d + \Lambda_{MC} \tilde{q}_{MC} \quad (12)$$

$$v_{IC} = \dot{q}_{IC}^d - \Lambda_{IC} \tilde{q}_{IC} - F_r z \quad (13)$$

$$a_{IC} = \dot{v}_{IC} = \dot{q}_{IC}^d - \Lambda_{IC} \dot{\tilde{q}}_{IC} - F_r \dot{z} \quad (14)$$

$$r_{IC} = \dot{q}_{IC} - v_{IC} = \dot{q}_{IC}^d + \Lambda_{IC} \tilde{q}_{IC} + F_r z \quad (15)$$

where  $K$ ,  $\Lambda_{IC}$ ,  $\Lambda_{MC}$ , and  $F_r$  are diagonal matrices with positive entries. Global asymptotic stability is proven in [27], so we can conclude that  $r$  and  $i$  converge to zero. Therefore,  $v_{MC} \rightarrow 0$  results in  $\dot{q}_{MC} + \Lambda_{MC} \tilde{q}_{MC} \rightarrow 0$  as shown in (11), which leads to asymptotic reference trajectory tracking for the MC joints; that is,  $q_M \rightarrow q_M^d$ . Based on (13) and its derivative,  $r_{IC} = 0$  and  $\dot{r}_{IC} = 0$  implies that

$$z = -F_r^{-1} (\dot{\tilde{q}}_{IC} + \Lambda_{IC} \tilde{q}_{IC}) \quad (16)$$

$$\dot{z} = -F_r^{-1} (\ddot{\tilde{q}}_{IC} + \Lambda_{IC} \dot{\tilde{q}}_{IC}) \quad (17)$$

Substituting (14) and (15) into the dynamic compensator (8) results in

$$F_r^{-1} \dot{\tilde{q}}_{IC} + (F_r^{-1} \Lambda_{IC} - AF_r^{-1} + k_d) \dot{\tilde{q}}_{IC} + (-AF_r^{-1} \Lambda_{IC} + k_p) \tilde{q}_{IC} = -k_f T_{IC} \quad (18)$$

where  $F_r$ ,  $k_d$ ,  $k_p$ , and  $k_f$  are chosen so that (16) matches the target impedance of (7). Given  $I$ ,  $b$ , and  $k$ , the dynamic compensator parameters  $F_r$ ,  $k_d$ ,  $k_p$ , and  $k_f$  are obtained as

$$\begin{aligned} F_r &= I^{-1} \\ k_d &= b - I\Lambda_{IC} + AI \\ k_p &= k + AI\Lambda_{IC}, \quad k_f = I_{m \times m} \end{aligned} \quad (19)$$

where  $I_{m \times m}$  denotes the identity matrix, and  $I$  denotes the inertia of the target impedance. In the control law of (9),  $T_e$  is assumed to be known. This assumption is valid since external forces can be measured by sensors and the Jacobian can be obtained from the manipulator kinematics. Note that we neglect the fast sensor dynamics in this study. We do not expect the sensor dynamics to affect the control, as confirmed by our experiment results in Section VII. The virtual control law leads to pure motion tracking for the active joints and achieves the target impedance for the semi-active joints. Impedance parameters  $I$ ,  $b$ , and  $k$  are tuned to regulate the dynamic compliance of the manipulator relative to  $T_{IC}$ .

### IV. EFFECT OF EXTERNAL FORCE ON ENERGY REGENERATION

In this section, we investigate the effect of external force on energy regeneration. External forces arise because of the interaction of the robot with the environment. There are several strategies for dealing with external force. For example, the external force could be regarded as a disturbance and canceled by the controller. Another option is to imposing a target impedance. It is important to consider how external force affects control, energy regeneration, and internal dynamics. According to the mixed PB tracking/impedance control law, the desired virtual control  $v_{e_j}$  for the  $j$ -th semi-active joint is derived from (9), which can be written as

$$v_{e_j} = Y_j(q, \dot{q}, a, v) \Theta - K_j r_j + T_{e_j} = \tau_j^e + T_{e_j} \quad (20)$$

where  $Y_j$  is the  $j$ -th row of the regressor matrix,  $\Theta$  is a parameter vector, and  $\tau_j^e = Y_j(q, \dot{q}, a, v) \Theta - K_j r_j$ . The change in the charge of the storage element is measured for each semi-active joint and multiplied by  $y_j$ . The result is then integrated over

a specified period of time to find the energy change in the capacitor [24], [27]. Substituting  $v_{c_j}$  into the internal energy balance equation gives

$$\Delta E_{s_j} = - \int_{t_1}^{t_2} \left( (\tau_j^e + T_{e_j}) \dot{q}_j + \frac{R_j}{a_j^2} (\tau_j^e + T_{e_j})^2 \right) dt \quad (19)$$

This shows that the change in the stored energy  $\Delta E_{s_j}$  is equal to the work done by a desired virtual control minus the energy dissipated due to the overall electrical resistance in the JM. If  $(\tau_j^e + T_{e_j}) \dot{q}_j < 0$ , then mechanical energy is transferred to the JM from the robotic link. Due to presence of  $q_j$  and  $\dot{q}_j$  in  $\tau_j^e$ , the sign of the work done by a desired virtual control depends on a nonlinear function of joint motion and velocity. Therefore, we might not recover energy even if the joint velocity is negative. Equation (19) shows that several parameters can affect the rate of energy storage, including the reference trajectory, external force, control gains, gear ratio, JM resistors, etc. In this paper, gear ratio, control gains, and JM resistances are fixed.

Equation (19) implies that a large external force may result in  $\Delta E_{s_j} < 0$ , which implies a loss of capacitor energy, since the dissipation part of (19) includes the square of the external force. On the other hand, a smaller external force can make  $\Delta E_{s_j} > 0$  and lead to energy regeneration. With the aid of impedance control it is possible to indirectly control the external force. Impedance control with a high target impedance leads to accurate joint tracking, large impact force magnitude, and possibly low energy regeneration. Conversely, low target impedance results in poor joint tracking, small impact force, and possibly high energy regeneration.

The impedance parameters  $I$ ,  $b$ , and  $k$  can be chosen to overcome external forces and obtain accurate tracking while decreasing energy regeneration. On the other hand, the parameters can also be tuned to accommodate external forces and improve regeneration at the expense of an increase in tracking error. Motion tracking accuracy and energy storage in the semi-active joints are thus conflicting objectives. Therefore, the problem of designing an impedance controller to track a desired joint trajectory and regenerate energy is a multi-objective optimization problem.

## V. MULTI-OBJECTIVE OPTIMIZATION

In this section, impedance parameter tuning to trade off joint tracking accuracy and energy regeneration is addressed with multi-objective optimization (MOO). In MOO problems, a set of solutions comprises alternative solutions called a Pareto set [34, Ch. 20]. In a Pareto set, no solution (Pareto point) is dominated by other solutions. The following equation defines a Pareto set for a problem with  $k$  minimization objectives:

$$P_s = \{x^* : [\exists x : f_i(x) \leq f_i(x^*) \text{ for all } i \in [1, k], \text{ and } f_j(x) < f_j(x^*) \text{ for some } j \in [1, k]]\} \quad (20)$$

where  $f_i(x)$  is the  $i$ -th objective function and  $x^*$  is a Pareto point. A Pareto point has the property that it is impossible to improve one of the objectives without degrading another. Selecting one

solution from among the Pareto set is a subjective decision on the part of the designer.

Evolutionary algorithms (EAs) have been recognized as powerful tools for solving MOO problems [26]. The non-dominated sorting genetic algorithm (NSGA) is known as an efficient algorithm for optimizing a wide range of real-world MOO problems [35]. During each generation of NSGA, the non-dominated individuals are moved to a subpopulation and assigned rank 1. Then, from the remaining individuals in the population, the new non-dominated individuals are assigned rank 2. This process is repeated until all individuals have been assigned a rank. The GA then selects individuals for recombination on the basis of their rank [34, Ch. 20]. Individuals with lower ranks are more likely than those with higher ranks to be selected for recombination. In this paper, biogeography-based optimization (BBO) is combined with non-dominated sorting to obtain the NSBBO algorithm. The main idea of BBO is explained in the following section.

### A. Biogeography-Based Optimization

We could choose any evolutionary algorithm for multi-objective optimization in this research. We have chosen BBO because of its demonstrated effectiveness and recent application for optimizing real-world problems [25]. BBO is a gradient-free, population-based algorithm that is based on mathematical models of species emigration, immigration, and distribution among islands [34, Ch. 14].

BBO is initialized with a set of randomly generated individuals (candidate solutions) in the search domain. The set of all individuals is called the population. BBO uses three main operators to improve the quality of the population at the next generation: (1) features (independent variables) are replaced between individuals based on their objective function values, (2) mutation is used to randomly change individuals to diversify the population, and (3) elitism is used to keep the best solutions in the population for the next generation [34, Ch. 3]. Mutation rate, the number of elites, the population size, and the number of generations are BBO parameters that are tuned to achieve good results for a specific problem.

### B. Objective Functions

The tracking error of the semi-active joints is one of the objectives, and is to be minimized. The stored energy in the ultracapacitors at the end of the simulation is the other objective, and is to be maximized. The following are the objective functions.

$$f_1 = \sum_{j=1}^m \sqrt{\frac{\sum_{i=1}^T (q_j(i) - q_j^d(i))^2}{T}} \quad (\text{radians}) \quad (21)$$

$$f_2 = \sum_{j=1}^m \frac{1}{2} C_j V_{C_j}^2 \quad (\text{Joules}) \quad (22)$$

where  $q_j(i)$  is the displacement of  $j$ -th semi-active joint at time sample  $i$ ,  $m$  is the number of semi-active joints, and  $f_1$  is the total RMS tracking error of the semi-active joints.  $T$  is the number

of sample points,  $V_{C_{j_f}}$  is the final capacitor voltage of the  $j$ -th semi-active joint, and  $f_2$  is the total ultracapacitor energy of the semi-active joints.

At this point we add a term to penalize candidate solutions whose capacitor voltage falls below a minimum threshold: such behavior implies an unacceptably fast energy loss:

$$\phi = 1000 \left| \min \left( V_{th}, \min_{j,t} V_{C_j}(t) \right) - V_{th} \right| \text{ (Volts)} \quad (23)$$

where  $V_{th}$  is the minimum voltage threshold, and  $V_{C_j}(t)$  is the time-varying capacitor voltage at the  $j$ -th semi-active joint. The factor 1000 in (23) is used to scale the significance of the penalty term  $\phi$ . The following MOO problem is solved by NSBBO:

$$\min_{I, b, k} \begin{bmatrix} \phi + f_1 \\ -f_2 \end{bmatrix} \text{ such that } q_j(t) \geq \rho_j \text{ for } j \in [1, m] \quad (24)$$

where  $\rho_j$  is a constant to constrain the  $j$ -th joint displacement for all  $t$ . Adding  $\phi$  to either  $f_1$  or  $-f_2$  would lead to a similar optimization result because in either cases the minimization cost would increase due to an infeasible solution with  $\phi > 0$ . Infeasible solutions are likely to be eliminated from the Pareto set in either case. Although  $\phi$  and  $f_1$  have different units, they are added with the assumption that implicit scaling is included in (23).

Our problem also includes  $m$  inequality constraints that account for joint displacement limits. Note that we do not enforce joint limit constraints with the controller. Instead we use the constraints to prevent the selection of infeasible solutions that violate the constraints. To handle the constraints in the optimization problem, we include the constraints as another objective [34, Ch. 19]:

$$f_3 = \sum_{j=1}^m \gamma_j G_j \quad (25)$$

where  $G_j$  is the constraint violation magnitude, which is defined as follows for our problem:

$$G_j = \left[ \max \left( 0, -\min_t (q_j(t) + \rho_j) \right) \right]^\beta \text{ for } j \in [1, m] \quad (26)$$

$\beta$  is a positive constant and  $\gamma_j$  is a function of the constraint violation magnitude:

$$\gamma_j = \begin{cases} 0 & \text{if } G_j = 0 \\ R_{j1} & \text{if } G_j \in (0, T_{j1}] \\ R_{j2} & \text{if } G_j \in (T_{j1}, T_{j2}] \\ \vdots & \\ R_{jp} & \text{if } G_j \in (T_{j,p-1}, \infty) \end{cases} \quad (27)$$

where  $p$  is the user-selected number of constraint levels, the  $T_{j_i}$  values are the constraint thresholds, and the  $R_{j_i}$  values are user-specified weights. This approach is known as the static penalty method [34, Ch. 19], is conceptually easy to implement, and ensures that infeasible solutions always have a worse objective function value than feasible solutions. NSBBO with the static penalty method is attractive because it retains infeasible solutions in the population. With this method, an infeasible solution can evolve into a feasible solution.

There are several other methods to handle constraints in optimization problems, such as the log barrier method [36]. However, the search domain of the log barrier method is restricted to feasible solutions because the penalty term is infinite for infeasible solutions. Therefore, the log barrier method ignores information from low-cost solutions that are only slightly infeasible. For this reason, we instead use a penalty method to benefit from the information provided by all solutions, including both feasible and infeasible solutions.

We perform manual tuning for the static penalty method parameters by first using a coarse grid search, followed by a fine grid search. In the coarse grid search, the performance of NSBBO is evaluated on a relatively wide range for the parameter values. The parameter values that provide the best NSBBO performance comprise the baseline for the fine grid search. In the fine grid search, NSBBO is evaluated on parameter values in the range  $\pm 10\%$  of their baseline values. The parameter values that provide the best NSBBO performance are the values that we use to present results here.

### C. Multi-Objective Optimization (MOO) Problems

We use NSBBO to find optimal impedance parameters and control gains for the semi-active joints with energy regenerative electronics:

$$\min_{I, b, k, \Lambda_{IC}, K_{IC}} \begin{bmatrix} \phi + f_1 \\ -f_2 \\ f_3 \end{bmatrix} \quad (28)$$

We consider two different cases: (1) constant impedance, and (2) time-varying impedance. In the first case, we search for the constant impedance parameters to minimize (28). In the second case, we search for time-varying impedance parameters to add flexibility to the control design. Instead of constant  $I$ ,  $b$ , and  $k$ , we use impedance parameters that are defined by cubic splines. Cubic spline interpolation is attractive for this application because it is fast, stable, accurate, and capable of fitting smooth curves. Mechanical limitations prevent robotic manipulators from responding to time-varying impedance parameters that have sharp and non-smooth profiles. Note that we use constant values for control gains  $\Lambda_{IC}$  and  $K_{IC}$  in both cases.

## VI. CASE STUDY: TRANSFEMORAL PROSTHESIS

We consider a 3-DOF robot with a prismatic-revolute-revolute joint structure, including two active joints and one semi-active joint, as illustrated in Fig. 2. The first 2 DOFs are active joints and emulate human hip displacement and thigh motion respectively, and the third DOF is a semi-active joint that represents the prosthetic knee. In a real-world prosthetic application, the control for the first 2 DOFs is provided by a human. However, the purpose of optimization in this paper is to find optimal control parameters for the prosthetic knee during test robot operation. The control system provides hip force and thigh torque so that the first 2 DOFs mimic human joint motion. The test robot was developed at Cleveland State University [37], [38].

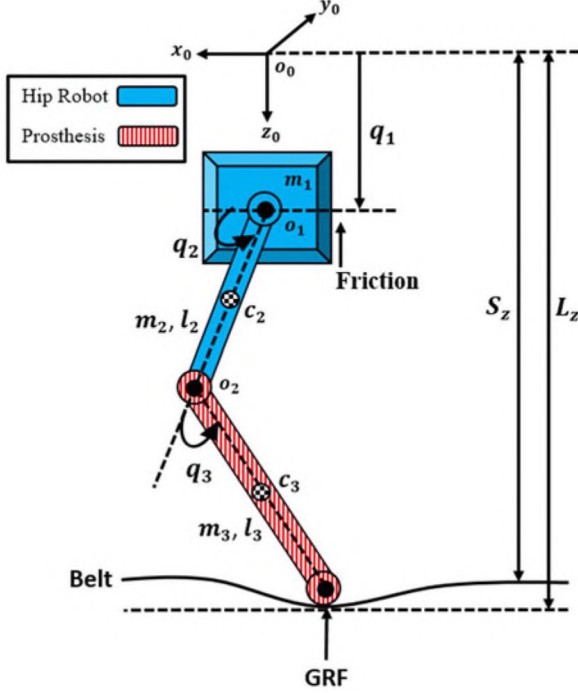


Fig. 2. The 3-DOF Cleveland State University prosthesis test robot [23], where the first 2 DOFs are active joints and emulate human hip displacement and thigh motion, and the third DOF is a semi-active joint that represents the prosthetic knee.

### A. Manipulator Specification

The first DOF is vertical hip displacement. The second and third DOFs are thigh and knee angle, respectively. Therefore, the vector of generalized joint displacements is  $[q_1 \ q_2 \ q_3]$ . The first two joints are active, and the knee is semi-active ( $n = 3, m = 1$ ). For simplicity, the JMs are ignored for the two active joints and they are directly driven by force and torque respectively. An ultracapacitor is used as the storage element in the semi-active knee JM. It has been shown that the capacitance value does not influence energy regeneration [39].

A point-foot model is used to model the interaction force.  $F_z$  is the vertical ground reaction force (GRF) and  $F_x$  is the GRF in the direction of walking.  $T_e$  is the combined effect of GRF on the three DOFs:

$$T_e = \begin{bmatrix} F_z \\ F_z (l_2 c_2 + l_3 c_{23}) - F_x (l_2 s_2 + l_3 s_{23}) \\ F_z (l_3 c_{23}) - F_x (l_3 s_{23}) \end{bmatrix} \quad (29)$$

where  $c_2$ ,  $c_3$  and  $c_{23}$  are shorthand for  $\cos(q_2)$ ,  $\cos(q_3)$ , and  $\cos(q_2 + q_3)$ , respectively. We use a treadmill with a constant velocity as the walking surface. The surface is modeled as a mechanical spring-like stiffness. The GRF is a function of treadmill belt deflection. The vertical coordinate of the foot is obtained from the forward kinematics:

$$L_z = q_1 + l_2 \sin(q_2) + l_3 \sin(q_2 + q_3) \quad (30)$$

where  $l_2$  and  $l_3$  are thigh and shank length, respectively. The treadmill belt deflection is  $d_z = S_z - L_z$ , where  $S_z$  is the vertical distance between the coordinate system origin and the

TABLE I  
PARAMETERS OF THE 3-DOF TEST ROBOT, THE SEMI-ACTIVE JM,  
AND THE POINT FOOT MODEL

	Symbol	Value	Units
<b>Manipulator Model</b>			
Mass of link 1	$m_1$	40.6	kg
Mass of link 2	$m_2$	8.57	kg
Mass of link 3	$m_3$	2.29	kg
Thigh length	$l_2$	0.425	m
Shank length	$l_3$	0.527	m
Length joint 1 to link 2 CG	$c_2$	0.09	m
Length joint 2 to link 3 CG	$c_3$	0.32	m
Rotary inertia of link 2	$I_{2z}$	0.435	kgm <sup>2</sup>
Rotary inertia of link 3	$I_{3z}$	0.0618	kgm <sup>2</sup>
Link 1 coulomb friction	$f$	83.3	N
Link 2 viscous damping	$b_2$	9.75	Nms
<b>Point-Foot Model</b>			
Treadmill belt stiffness	$\delta$	37000	Nm <sup>-1</sup>
Treadmill friction factor	$\gamma$	0.25	unitless
Velocity scaling factor	$v_0$	0.01	ms <sup>-1</sup>
Treadmill velocity	$v_t$	1.25	ms <sup>-1</sup>
Standoff Constant	$S_z$	0.918	m
<b>Semi-Active JM</b>			
JM gear ratio	$n_3$	50	unitless
Storage capacitance	$C_3$	500	F
Ultracapacitor initial voltage	$V_{C_3}$	20	volt
DC machine motor constant	$\alpha_3$	0.06	Nm/A
DC machine series resistance	$R_{r,3}$	0.1	$\Omega$
Additional series resistance	$R_{s,3}$	0	$\Omega$
Viscous damping (motor side)	$b_3$	0	Nms
Rotary inertia (motor side)	$m_3^*$	1.0E - 5	kgm <sup>2</sup>

CG Stands for Center of Gravity.

treadmill belt, and is called the standoff constant. GRF along the  $z$ -axis and  $x$ -axis is

$$F_z = \begin{cases} 0 & \text{for } L_z \leq S_z \quad (\text{swing phase}) \\ -\delta d_z & \text{for } L_z > S_z \quad (\text{stance phase}) \end{cases}$$

$$F_x = - \left( \frac{1 - \exp(-v_r/v_0)}{1 + \exp(-v_r/v_0)} \right) \gamma F_z \quad (31)$$

where  $F_x$  is approximated by Coulomb friction [40].  $\delta$  and  $\gamma$  are the belt stiffness and friction coefficient, respectively [29].  $v_0$  is a scaling factor, and  $v_r$  is the relative velocity of the foot with respect to the treadmill and is computed as

$$v_w = -\dot{q}_2 (l_2 \sin(q_2) + l_3 \sin(q_2 + q_3)) - \dot{q}_3 l_3 \sin(q_2 + q_3)$$

$$v_r = v_w - v_t \quad (32)$$

where  $v_w$  is the velocity of foot in the direction of walking, which is obtained from forward kinematics, and  $v_t$  is the treadmill velocity. The parameters of the 3-DOF prosthesis test robot, the semi-active JM, and the point-foot model are reported in Table I and are within the range of commercially available devices. As seen in Table I and (30), if the leg is straight ( $q_2 = \pi/2, q_3 = 0$ ), then  $L_z$  is larger than  $S_z$  and is equal to  $q_1 + l_2 + l_3$ . Based on (31), when  $L_z$  is larger than the standoff constant (stance phase), GRF is nonzero; this observation illustrates the consistency of the force model. The robot regressor and parameter vector are given in [23]. As shown in Table I,

TABLE II  
CONTROLLER GAINS FOR THE TWO ACTIVE JOINTS

Hip Joint Gain	Value
$\Lambda_{MC,1}$	155
$K_{MC,1}$	155
Thigh Joint Gain	
$\Lambda_{MC,2}$	155
$K_{MC,2}$	150
Compensator Gain	
$A$	-20

the overcharge control resistor  $R_{s3}$  is bypassed, so we assume  $s_3 = 0$  for the remainder of the paper.

### B. Control Parameters

The desired virtual control is obtained from mixed PB tracking/impedance control, where the first two components are active force and torque for the upper joints (hip displacement and thigh angle), and the third component is the virtual control  $a_3 r_3 y_3 / R_3 C_3$ . The control objective is motion control for the upper joints and impedance control for the knee joint. The controller gains and parameters of the first two active joints are shown in Table II. The impedance parameters ( $I$ ,  $b$ , and  $k$ ) and control gains ( $\Lambda_{IC}$ ,  $K_{IC}$ ) of the knee joint will be obtained by NSBBO. An able-bodied subject with weight 78 kg and height 1.83 m walking at normal speed was recorded at the Motion Studies Laboratory of the Cleveland Department of Veterans Affairs Medical Center (VAMC) [41] and is used for the reference trajectory.

### C. NSBBO Parameters

In this case study, the prosthetic knee is the only semi-active joint. As mentioned in Section V-C, NSBBO is used to find the impedance parameters and control gains for the knee joint to minimize the RMS error of knee joint tracking and maximize the change in capacitor energy. The purpose of the first objective function is to achieve a symmetric and near-normal gait for the amputee. This objective is attractive in that symmetric gait has been shown to alleviate ancillary health problems in amputees, and amputees prefer to walk with a symmetric gait [42], [43]. The purpose of the second objective function is to regenerate energy in the ultracapacitor. This objective is attractive in that a powered robotic leg prosthesis has been shown to provide limited hours of continuous walking on a single battery charge. For instance, the powered prosthetic knee/ankle system in [44] can provide about 1.5 hours of continuous walking at normal speed.

The search domains of the impedance parameters and control gains are shown in Table III. The nominal values of the impedance parameters for good tracking at the knee joint are taken from [33], and the search space is large enough to include the nominal values and a significant region around them. We increased the search domain if the optimum solutions found

TABLE III  
OPTIMIZATION SEARCH DOMAIN FOR THE IMPEDANCE PARAMETERS AND CONTROL GAINS

Parameter	Minimum Value	Maximum Value
$I$	1.0 E - 1	5.0 E + 1
$b$	1.0 E + 0	7.0 E + 3
$k$	1.0 E + 0	6.0 E + 4
$\Lambda_{IC}$	1.0 E + 0	4.0 E + 3
$K_{IC}$	1.0 E + 0	4.0 E + 3

TABLE IV  
NSBBO TUNING PARAMETERS USED FOR OPTIMIZATION OF THE PB TRACKING/IMPEDANCE CONTROLLER

NSBBO Parameters	Value
Mutation rate	0.04
Number of elites	2
Population size	50
Number of generations	400

by NSBBO were close to the search domain boundary. We narrowed the search domain if the optimum solution was far from the boundary. This approach led to the domains shown in Table III.

The NSBBO parameters were manually tuned to achieve satisfactory results and are shown in Table IV. To tune the parameters, we performed a sensitivity analysis of NSBBO performance to each parameter, one at a time, to find a local optimum of NSBBO performance with respect to each parameter. EA parameter tuning is scientific in that we vary the parameters to find locally optimum values, but it is also an art that is based on EA experience that provides intuition for how to vary the parameters [34], [45].

Previous research measured the range of motion (ROM) of the body joints for various activities [46, Ch. 12], [47], [48]. In [47], maximum knee flexion and extension for level walking is measured for two age groups of 60 healthy subjects. Maximum knee flexion of  $66^\circ \pm 4^\circ$  and  $69^\circ \pm 5^\circ$  is reported for young and old age groups, respectively. Maximum knee extension of  $-3^\circ \pm 4^\circ$  and  $-6^\circ \pm 5^\circ$  is reported for young and old age groups, respectively. Aging leads to loose tendons and ligaments, and subsequently larger and undesirable knee hyperextension for older subjects. However, we use a conservative value for  $\rho_3$  such that both young and old subjects would feel comfortable when wearing the prosthesis as controlled here. Therefore, the inequality  $q_3 \geq \rho_3 = -2.3^\circ$  is used as an MOO constraint to prevent knee hyperextension.

The following tuning parameters are used in the static penalty method.

$$\beta = 1.5, p = 6, [R_{31} R_{32} \cdots R_{36}] = [1 \ 3 \ 10 \ 20 \ 50 \ 100],$$

$$[T_{31} T_{32} \cdots T_{35}] = 0.01 \times [1 \ 2 \ 4 \ 6 \ 9] \quad (33)$$

$\beta = 1.5$  is obtained by manual tuning for good MOO performance, which is consistent with  $\beta \approx 2$  as reported in [34, Ch. 19].  $p = 6$  is the number of constraint levels, and is chosen as a

tradeoff between algorithmic flexibility and constraint-handling simplicity. In summary, we use NSBBO to solve the MOO problem in (28) for a 3-DOF robotic manipulator with energy regenerative electronics.

## VII. RESULTS AND DISCUSSION

This section first presents simulation results with constant impedance in Section VII–A, then presents simulation results with time-varying impedance in Section VII–B, then compares simulation results in Section VII–C, then presents experimental results in Section VII–D, and finally discusses potential improvements and limitations in Section VII–E.

### A. Constant Impedance

We first run NSBBO with constant impedance parameters for 10 independent trials, and achieve similar Pareto fronts each simulation, thus confirming the repeatability of NSBBO for this application. Fig. 3 shows the non-dominated Pareto points obtained from all 10 MOO trials. For clarity we illustrate 2-dimensional projections of the Pareto front instead of the 3-dimensional view. Fig. 3(a) shows RMS knee angle tracking error  $f_1$  and change in capacitor energy  $E_0 - f_2$ , where  $E_0$  is the initial capacitor energy. Note that no solutions violate the penalty term, so  $\phi = 0$  for all solutions. Fig. 3(a) verifies the conflicting nature of the two objective functions. Fig. 3(b) illustrates the change in energy and the inequality constraint violation magnitude  $f_3$ . Fig. 3(c) shows the inequality constraint violation and the knee angle tracking error. Fig. 3 verifies that Pareto points with high energy regeneration tend to have large knee angle tracking error and large inequality constraint violation magnitude.

After Pareto points are obtained, the user needs to subjectively select a single solution for implementation. A pseudo-weight approach is used here to make the selection convenient. For each Pareto point, a weight vector  $W$  with a dimension equal to the number of objectives is calculated as follows [49]:

$$w_i = \frac{(f_i^{\max} - f_i) / (f_i^{\max} - f_i^{\min})}{\sum_{m=1}^M (f_m^{\max} - f_m) / (f_m^{\max} - f_m^{\min})} \quad i = 1, 2, \dots, M$$

$$W = [w_1 \ w_2 \ \dots \ w_M] \quad (34)$$

where  $M$  is the number of objectives, and  $f_i^{\max}$  and  $f_i^{\min}$  are the maximum and minimum value of the  $i$ -th objective function (taken among all Pareto points). Note that the sum of the components of  $W$  is 1. Fig. 3 shows the 2-dimensional projection of the Pareto front, where we label some Pareto points with various weight vectors as representative points. Table V shows the impedance parameters for the Pareto points that are labeled in Fig. 3. The labeled points are highlighted in red in order to be easily identified and cross-referenced with the points in Table V.

The solution with pseudo-weight  $W = (0.5, 0, 0.5)$  has the minimum knee tracking error 0.0009 rad, the maximum energy loss  $-37.75$  J, and no inequality constraint violation. In contrast,  $W = (0, 1, 0)$  has the worst tracking error 0.0461 rad, the highest energy gain 263.1 J, and the highest inequality constraint violation magnitude 0.0541. The initial energy of the

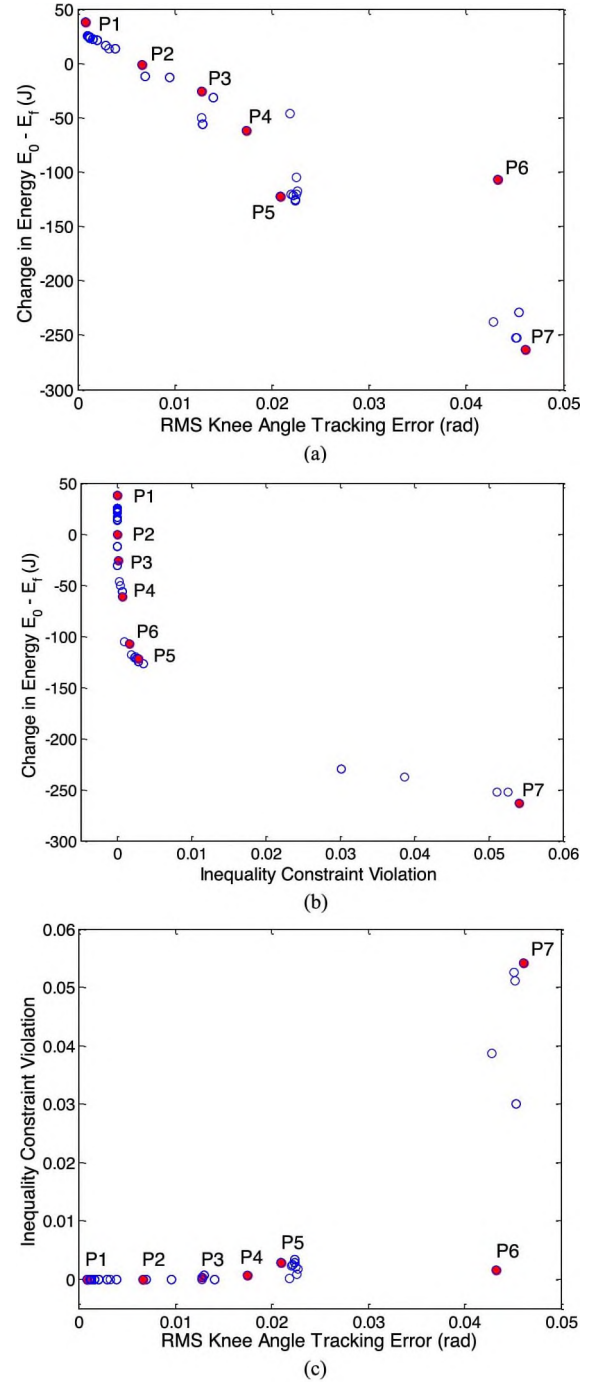


Fig. 3. Two-dimensional projection of Pareto points for the MOO problem with three objective functions. (a) 2-D projection of the Pareto front, where the vertical axis is the change in the capacitor energy after 10 seconds, and the horizontal axis is the knee tracking error. The initial capacitor energy is 100 kJ, and  $E_f$  denotes the final capacitor energy  $f_2$ , so the Pareto points above 0 lose energy and points below 0 gain energy. None of the Pareto points violate the penalty term, so  $\phi = 0$ . (b) 2-D view of  $E_0 - f_2$  with respect to  $f_3$ . (c) 2-D view of  $f_3$  and  $f_1$ .

capacitor is 100 kJ. Tracking is excellent for  $W = (0.5, 0, 0.5)$  at the expense of energy loss, while energy regeneration is positive for  $W = (0, 1, 0)$  at the expense of degradation in the joint angle tracking and knee hyper-extension of 6.23 degrees.

TABLE V  
KNEE TRACKING ERROR  $e_{\text{knee}}$ , ENERGY CHANGE, AND MAGNITUDE OF INEQUALITY CONSTRAINT VIOLATION FOR SELECTED PARETO POINTS FROM FIG. 3, ALONG WITH CORRESPONDING IMPEDANCE PARAMETERS AND CONTROL GAINS

Pareto point	pseudo weight	$e_{\text{knee}}$ (rad)	energy (J)	constraint violation	$I$ (Kgm <sup>2</sup> )	$b$ (Nms)	$k$ (Nm)	$K_{IC}$	$\Lambda_{IC}$
$P_1$	(0.50, 0.00, 0.50)	0.0009	-37.75	0.00 E + 0	1.8569	5145.6	59523	3159.2	867.49
$P_2$	(0.44, 0.06, 0.50)	0.0066	+0.897	0.00 E + 0	22.896	622.03	19176	1965.4	164.69
$P_3$	(0.36, 0.15, 0.49)	0.0128	+24.60	3.78 E - 4	12.892	68.463	59644	2291.4	2358.7
$P_4$	(0.32, 0.17, 0.51)	0.0174	+61.55	6.28 E - 4	12.892	68.463	24514	1965.4	164.68
$P_5$	(0.27, 0.26, 0.47)	0.0209	+122.3	2.80 E - 3	21.440	68.463	59644	3343.9	164.69
$P_6$	(0.04, 0.32, 0.64)	0.0440	+101.7	1.60 E - 3	23.896	70.478	19176	2275.2	3157.3
$P_7$	(0.00, 1.00, 0.00)	0.0461	+263.1	5.41 E - 2	47.644	68.463	59644	1965.4	164.69

Fig. 4 illustrates mixed tracking/impedance control performance for three Pareto points:  $W = (0.5, 0, 0.5)$ ,  $W = (0, 1, 0)$ , and  $W = (0.36, 0.15, 0.49)$ . The Pareto point for  $W = (0.36, 0.15, 0.49)$  in Fig. 4 is a suitable tradeoff. It provides positive energy regeneration, tracking error of 0.0128 rad, and constraint violation of 3.78E-4. There are other Pareto points with similar characteristics in Fig. 3, but we choose Pareto point  $W = (0.36, 0.15, 0.49)$  as representative. We choose  $P_3$  because it was the first Pareto point in Table V with considerable positive energy gain and smaller tracking error. However, we could choose other similar Pareto points with similar properties, depending on the priority of the control objectives.

For clarity, Fig. 4 spans only five seconds and the desired trajectories are indicated with a thick gray line. As expected, in Fig. 4(a) and (b) near-perfect tracking is achieved for hip position and thigh angle for all pseudo-weight combinations. However, in Fig. 4(c) external force is handled by impedance control for the knee joint, which results in a deviation from the reference trajectory. For clarity, Fig. 4(d) zooms in on the knee joint angle for a single gait cycle.

Fig. 5(a) shows ultracapacitor voltage for the three selected solutions. The Pareto point  $W = (0.5, 0, 0.5)$  loses energy so the capacitor voltage decreases.  $W = (0.36, 0.15, 0.49)$  shows a slight voltage increase.  $W = (0, 1, 0)$  has relatively high energy regeneration and a corresponding capacitor voltage increase. Fig. 5(b) shows GRF along the z-axis for the three selected solutions. The resulting GRF is similar to able-bodied GRF in shape and magnitude, despite the fact that a simple point foot model is used [37].

$W = (0.5, 0, 0.5)$  is not a suitable solution because of its high energy loss. Although  $W = (0, 1, 0)$  results in energy regeneration, it is not a suitable solution since tracking is poor in stance phase, and it results in chattering and abnormal knee hyperextension of approximately 6 degrees. The Pareto point with  $W = (0.36, 0.15, 0.49)$  is a suitable trade-off since it has near-perfect tracking in swing phase and acceptable tracking during stance phase with negligible chattering but positive energy change. “Acceptable” tracking is quantified by noting that intrasubject variability of knee angle for an able-bodied subject is 0.033 rad [50]. We assume that the tracking performance for the prosthetic knee is acceptable if the RMS error is less than intrasubject knee angle variability. The maximum knee hyper-extension for  $W = (0.36, 0.15, 0.49)$  is 2.35 degrees, which slightly violates the inequality constraint but is normal

for healthy subjects [47]. We choose the Pareto solution corresponding to  $W = (0.36, 0.15, 0.49)$  to achieve our desired control objectives, which are trajectory tracking and energy regeneration for the knee joint. However, one could choose other solutions in Fig. 3 with similar properties, depending on the priority of the control objectives.

Fig. 6 shows the hip and thigh control signals for the selected Pareto point  $W = (0.36, 0.15, 0.49)$ . The average magnitudes of able-bodied hip force and thigh torque are in the range -800 to 200 N and -50 to 100 Nm, respectively [50]–[52]. The peak magnitudes of hip force and thigh torque in Fig. 6, ignoring instantaneous spikes in thigh torque, are two times greater than in able-bodied human subjects. This is partially due to the fact that we use large control gains for the active joints to achieve pure motion tracking with small error on the order of 1E-5 rad. Another reason is the differences between the dynamics of the prosthesis test robot and human walking. As a result, we have different forces and torques. These differences do not cause concern because in our application hip force and thigh torque are provided by the prosthesis test robot, while in amputee applications they are provided by human subjects. Future work with amputee subjects will need to ensure that the torques that are available from the knee motor can provide a good balance between angle tracking and regeneration with human-generated hip and thigh motions. A final reason for the large hip force and thigh torque is the difference between the dynamics of the prosthesis and the human knee/shank/ankle/foot system. For example, as in most transfemoral prostheses, there is no ankle push-off in our simulated prosthesis.

We constrain the modulating input to  $|r_3| \leq 1$  to account for amplifiers whose output voltage is limited to the supply voltage. A fixed-ratio boost stage in series with our modulating element could be used to relax this constraint, but our results indicate that this is not necessary for normal walking,  $r_3$  is within the specified range and is illustrated in Fig. 7. This reveals that the designed controller for normal walking would be realistic for use in real-world prosthesis applications. It will be of great interest to investigate the performance of the control system for various walking activities in future research. Equation (6) shows that  $r_3$  is an adjustable parameter that has a direct relationship with the knee joint control signal. Fig. 7 shows that a small  $r_3$  is required when the knee joint displacement is small, while a higher  $r_3$  is required when the knee joint displacement is large.

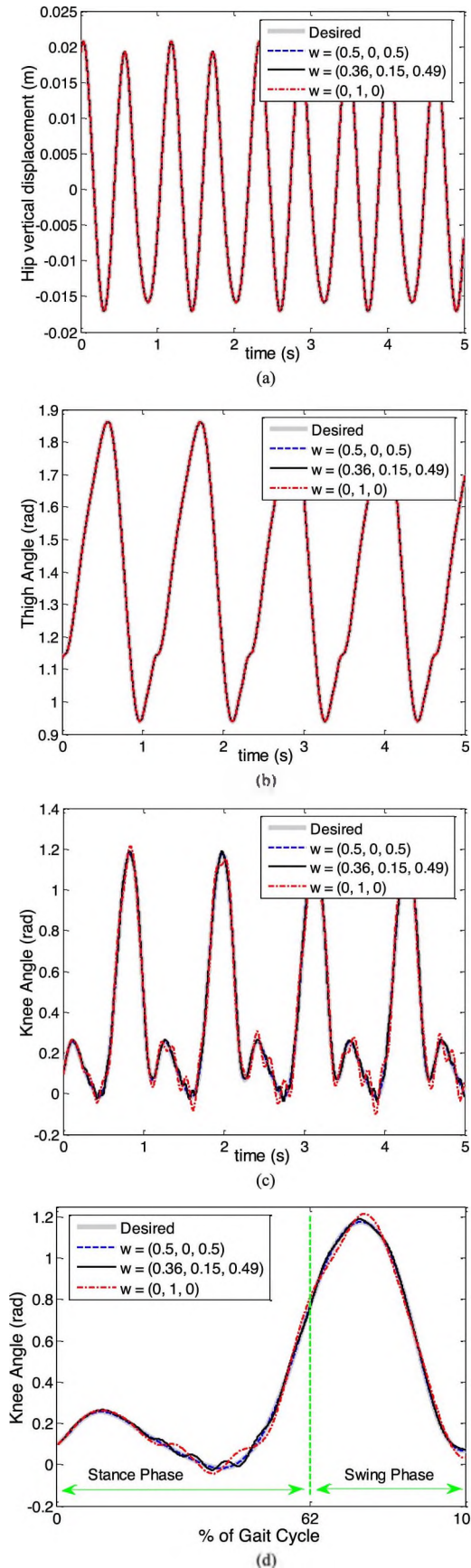


Fig. 4. (a) Vertical hip displacement, (b) thigh angle, (c) knee angle, and (d) zoomed knee angle for a single cycle.

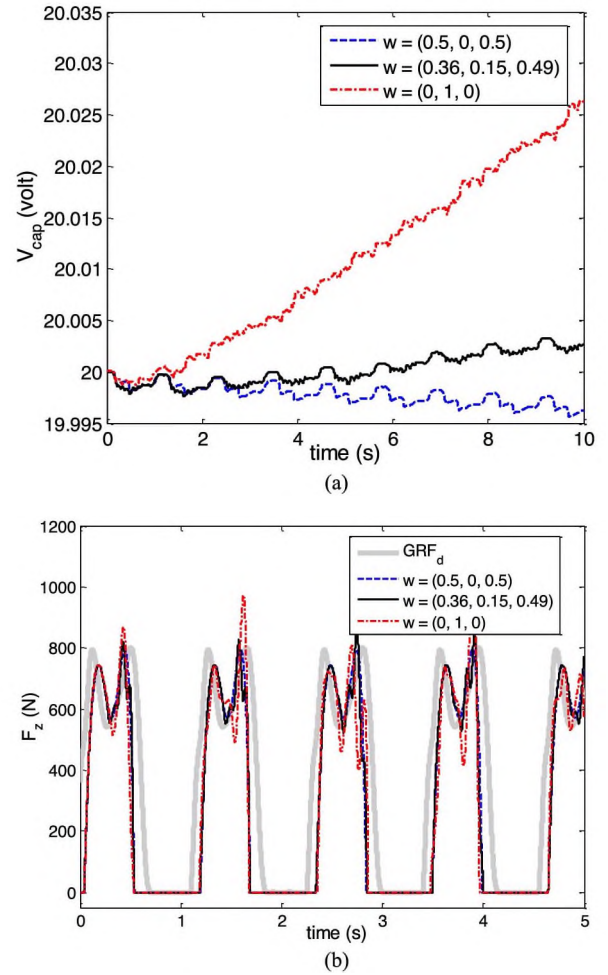


Fig. 5. (a) Ultracapacitor voltage, and (b) GRF along the z-axis for three selected solutions.

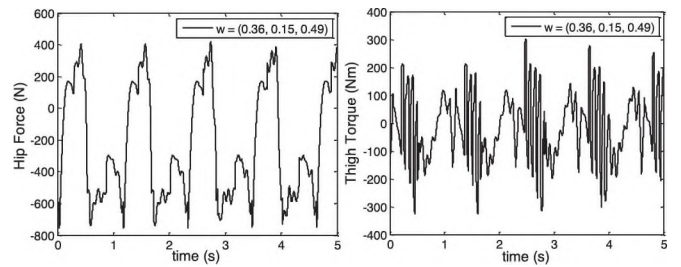


Fig. 6. Hip and thigh control signal for the selected Pareto solution  $W = (0.36, 0.15, 0.49)$ .

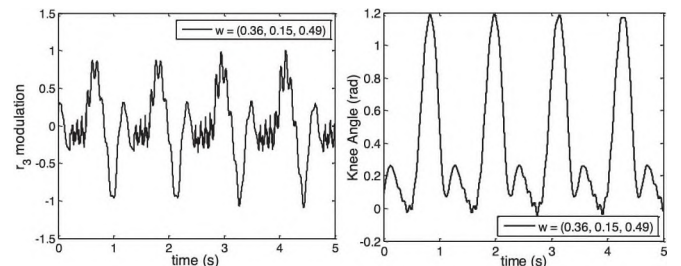


Fig. 7. Knee control signal and angle for the selected Pareto solution  $W = (0.36, 0.15, 0.49)$ .

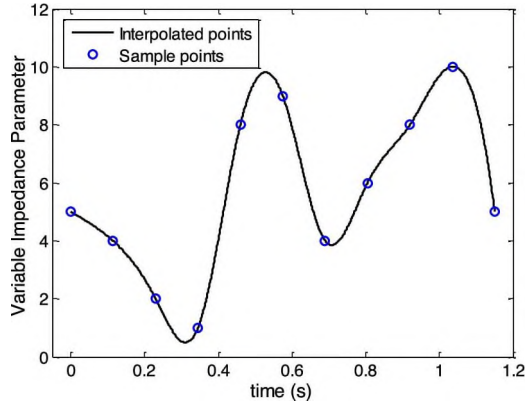


Fig. 8. An example of time-varying impedance with  $l = 10$  knots, where the impedance is generated by a cubic spline through the knots.

### B. Time-Varying Impedance

The preceding section showed that constant impedance results in chattering in the knee joint during stance. Although the amount of chattering is small enough that knee tracking error is small, the amputee may not feel comfortable with such chattering. Therefore, time-varying impedance is suggested here. Time-varying impedance can add flexibility to the control design, diminish chattering, and better satisfy the control objectives.

Each impedance parameter should be variable and periodic with frequency  $w_n = 5.46$  rad/s, which is the frequency of the walking gait. We divide each gait cycle into  $l$  equal time slots, and generate  $l$  impedance values, which we use as spline knots. Then the value of each impedance parameter at any time instant is determined by cubic spline interpolation through the knots. MOO finds the optimum values for the  $l$  knots to minimize the objectives. Fig. 8 shows an example of time-varying impedance with  $l = 10$  knots.

The control gains and parameter search domains are the same as in Tables II and III. The inequality constraint and its parameters are the same as in Section VI-C. A large value for  $l$  results in more flexibility but makes the optimization problem more computationally expensive. Additionally, the performance of global optimization algorithms degrade as dimensionality increases [34].

A tradeoff between simplicity and flexibility is required. In this research, we use  $l = 10$  so there are 10 coefficients to be optimized for each impedance parameter, and we optimize two control gains, for a total of 32 independent variables. Since the number of independent variables is significantly larger than in the previous section, we increase the number of NSBBO generations to 700. The other NSBBO tuning parameters are the same as in Table IV.

We run NSBBO for 10 independent trials. The Pareto front of Fig. 9 is obtained and is compared to the Pareto front with constant parameters. Fig. 9 shows the change in capacitor energy  $E_0 - f_2$  and RMS knee angle tracking error  $f_1$ . The range of inequality constraint violation magnitude  $f_3$  for the knee angle is also illustrated in this figure.

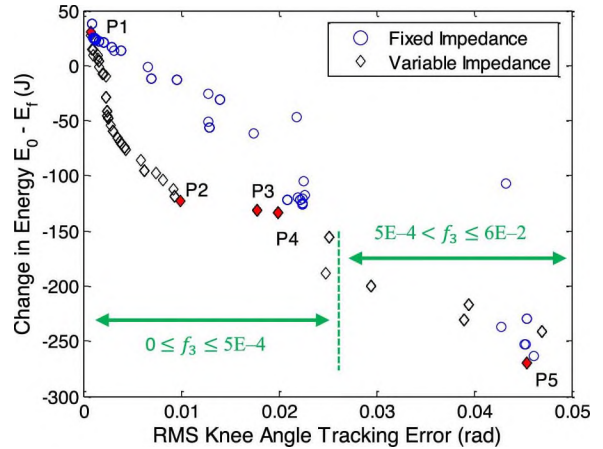


Fig. 9. Two-dimensional projections of Pareto fronts obtained with time-varying and constant impedance values. The range of the inequality constraint violation magnitude  $f_3$  is shown in green.

TABLE VI  
PSEUDO-WEIGHT, KNEE TRACKING ERROR, ENERGY CHANGE, AND MAGNITUDE OF INEQUALITY CONSTRAINT VIOLATION FOR FIVE SELECTED PARETO POINTS FROM FIG. 9 WITH TIME-VARYING IMPEDANCE

Pareto point	pseudo weight	$e_{knee}$ (rad)	energy (J)	constraint violation
$P_1$	(0.50, 0.00, 0.50)	0.0008	-9.531	0.00 E + 0
$P_2$	(0.34, 0.24, 0.42)	0.0100	+122.8	0.00 E + 0
$P_3$	(0.28, 0.27, 0.45)	0.0178	+131.2	0.00 E + 0
$P_4$	(0.27, 0.28, 0.45)	0.0199	+133.5	4.87 E - 4
$P_5$	(0.00, 1.00, 0.00)	0.0452	+270.3	5.04 E - 2

The Pareto points with time-varying impedance do not violate the penalty term, so  $\phi = 0$  for all solutions. However, some Pareto points violate the knee angle inequality constraint. Fig. 9 verifies that the constraint violation magnitude increases as the knee joint tracking error increases. The Pareto points with tracking error less than 0.03 rad slightly violate the inequality constraint; in these cases the knee angle is sometimes less than zero, but always greater than  $-2.69$  degrees. The Pareto points with tracking error greater than 0.03 rad violate the constraint; the maximum knee hyperextension is between 2.7 and 6 degrees in these cases. Pareto points with tracking error less than 0.03 rad would be suitable for both young and old subjects, and Pareto points with tracking error between 0.03 and 0.05 rad would be acceptable for old subjects (see Section VI-C). Pareto points with maximum knee joint hyperextension larger than 6 degrees would not be practical. Table VI shows the pseudo-weights and objective function values for the five representative Pareto points with time-varying impedance that are labeled in Fig. 9. Tables V and VI verify that the inequality constraint violation is smaller for solutions with time-varying impedances than with constant impedances.

Fig. 9 shows that solutions with time-varying impedance dominate solutions with constant impedance. Note that the nature of a Pareto front is to provide multiple candidate solutions that satisfy the MOO problem as in Fig. 9. A fair comparison of constant and time-varying impedance cannot rely on a com-

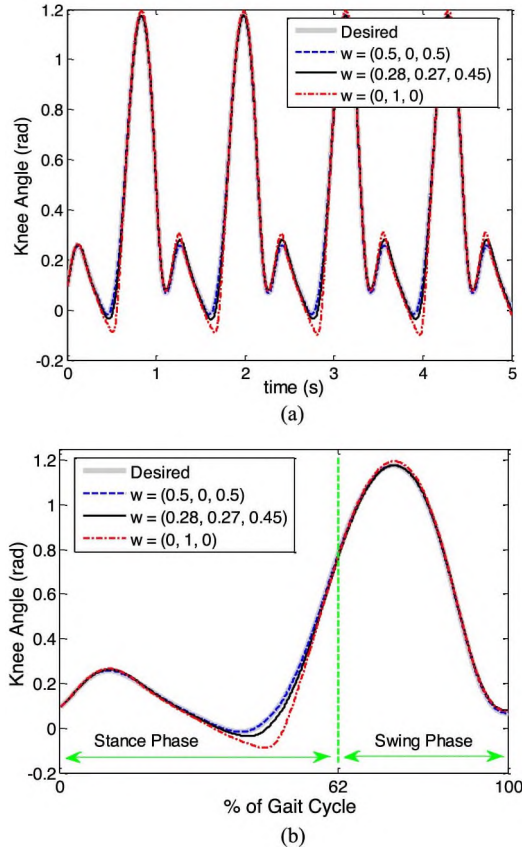


Fig. 10. (a) Knee joint angle for three solutions with time-varying impedance, and (b) zoomed knee angle for a single cycle.

parison of a single solution from each Pareto front, because the selected solution from each Pareto front might not outperform the other one with respect to all objective functions. Therefore, Section VII–C instead applies two systematic approaches to compare the Pareto fronts obtained with time-varying and constant impedance.

The solution with pseudo-weight  $W = (0.5, 0, 0.5)$  has the minimum knee tracking error 0.0008 rad, the worst energy change  $-9.531$  J, and no inequality constraint violation. On the other hand,  $W = (0, 1, 0)$  has the worst tracking error 0.0452 rad, the highest energy gain 270.3 J, and the worst inequality constraint violation magnitude 0.0504.  $W = (0.28, 0.27, 0.45)$  is a tradeoff solution with tracking error 0.0178 rad, positive energy gain, and no constraint violation. The Pareto point  $W = (0.28, 0.27, 0.45)$  is a suitable solution that provides reasonable performance for all three objective functions. There are other Pareto points with similar characteristics in Fig. 9, but we choose Pareto point  $W = (0.28, 0.27, 0.45)$  as a representative tradeoff.

We achieve near-perfect tracking for hip position and thigh angle for all pseudo-weight combinations. External force is handled by impedance control for the knee joint, and results in a deviation from the reference trajectory as illustrated in Fig. 10(a). For clarity, Fig. 10(b) zooms in on the knee joint angle for one gait cycle. Fig. 11 shows ultracapacitor voltage for three pseudo-weight combinations.  $\Delta E_{s3}$  is neg-

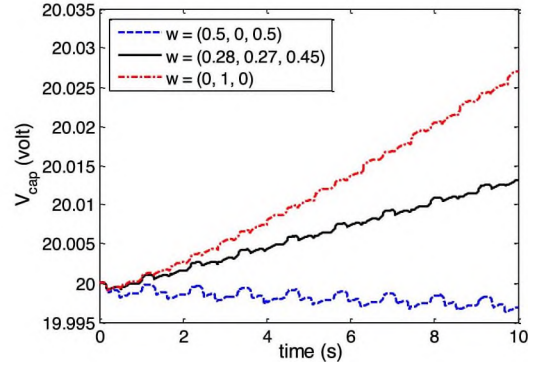


Fig. 11. Ultracapacitor voltage for three solutions with variable impedance.

TABLE VII  
COMPARISON OF PARETO FRONTS WITH CONSTANT IMPEDANCE  $PF_C$ , AND TIME-VARYING IMPEDANCE  $PF_V$ , USING NORMALIZED HYPERVOLUME AND RELATIVE COVERAGE

Pareto front	$NP$	Number of dominated points	Relative Coverage	Normalized Hypervolume
$PF_C$	134	128	95.5%	$-9.387$
$PF_V$	110	0	0.00%	$-24.23$

ative for  $W = (0.5, 0, 0.5)$  (energy loss), and positive for  $W = (0, 1, 0)$  and  $W = (0.28, 0.27, 0.45)$  (energy gain).

Recall that Fig. 4(c) showed that solutions with constant impedance resulted in undesirable chattering in the knee angle during stance phase. However, Fig. 10 shows that solutions with time-varying impedance do not result in chattering, and the knee angle deviates only slightly from the desired reference trajectory to regenerate energy. This is the primary benefit in using time-varying impedance. The average magnitude of each time-varying impedance parameter is close to the constant impedance parameters that were found in the previous section.

### C. Comparison of Pareto Fronts

A comparison of the Pareto front with constant impedance parameters  $PF_C$ , and the Pareto front with time-varying parameters  $PF_V$ , is conducted here using Pareto front hypervolume and relative coverage. These methods are popular for evaluating the quality of a Pareto front [34], [53]. The Pareto front normalized hypervolume is computed as

$$\text{Normalized Hypervolume} = \frac{\sum_{j=1}^{NP} \prod_{i=1}^M f_i}{NP} \quad (35)$$

where  $M$  is the number of objectives,  $f_i$  is the value of the  $i$ -th objective function, and  $NP$  is the number of Pareto points. Another way to compare Pareto fronts is to compute relative coverage. This metric is determined by the number of solutions in the first Pareto set that are weakly dominated by at least one solution in the second Pareto set [34], [53].

A smaller number for normalized hypervolume and relative coverage indicates better performance. Table VII shows the

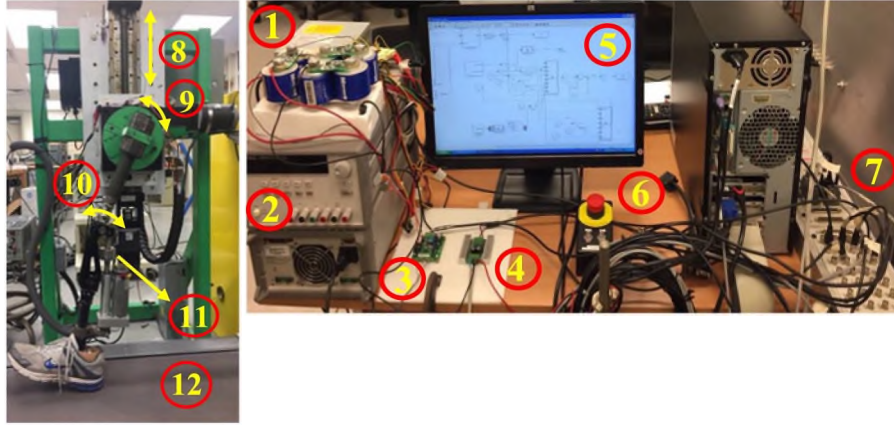


Fig. 12. Experimental setup for the 3-DOF Cleveland State University test robot and prosthesis. The components used in the experimental setup are: 1) capacitor bank, 2) initial capacitor bank charger, 3) load cell driver, 4) syren10 servo amplifier, 5) PC running control system, 6) emergency stop, 7) data acquisition interface, 8) hip vertical displacement, 9) thigh angular motion, 10) knee angular motion, 11) load cell, and 12) treadmill.

normalized hypervolume and relative coverage of  $PF_C$  and  $PF_V$ . Note that the number of Pareto points is an output of the optimization algorithm. The number of Pareto points depends on the characteristics of the problem, the inherent randomness of the evolutionary optimization algorithm, and the problem dimension. For instance, as the problem dimension increases the search space becomes larger, and therefore the optimization algorithm typically finds fewer solutions.

Table VII shows that none of solutions in  $PF_V$  are weakly dominated by any solutions in  $PF_C$ , while 95.5% of solutions in  $PF_C$  are weakly dominated by at least one Pareto point in  $PF_V$ . In addition, the normalized hypervolume of  $PF_V$  is smaller than that of  $PF_C$ . These results clearly indicate that time-varying impedance performs better than constant impedance, and therefore provide better tracking accuracy and energy storage.

Simulation results for time-varying impedance show that the tradeoff solution can recover 131.2 J during 10 seconds of normal walking. Assuming that one gait cycle is approximately 1.15 seconds, the amount of recovered energy in each stride would be 16.18 J. Note that in addition to this surplus energy, which could be provided to a prosthetic ankle, the ultracapacitor could provide the energy required by the knee joint for an unlimited amount of normal walking. The ankle joint of an able-bodied person requires about 17.8 J during normal walking [21]. Therefore, the tradeoff solution allows the possibility of transferring surplus energy at the knee to the ankle joint. This result has the potential to significantly reduce power requirements in a powered prosthesis.

Contrary to solutions with constant impedance, time-varying impedance results in knee angle tracking without high frequency oscillations. Although some solutions may lead to abnormal knee hyperextension in our simulations, we would not select them from the Pareto set for practical control solutions. In addition, a real prosthetic leg would include a mechanical stop to prevent hyperextension. There could be unusual and unexpected walking scenarios in real-world applications that could result in hyperextension. In such cases, the controller would have to be robust enough to react to the resultant impact force.

Further development and experiments will be required to study this problem.

#### D. Experimental Results

We perform an experimental test on the 3-DOF prosthesis test robot discussed in Section VI to demonstrate: (1) the conflicting nature of trajectory tracking and energy regeneration; and (2) the feasibility of energy regeneration in a prosthetic knee powered by ultracapacitors. The first two DOFs, hip displacement and thigh angle, are motion controlled and powered by external sources, while the third DOF, prosthetic knee angle, is semi-active and impedance controlled. Translational and angular motions are measured with optical encoders. External force at the knee joint is measured with a load cell and is used as feedback in the control system. A capacitor bank powers the knee joint, while the upper joints are powered by external sources. The capacitor bank has six 650 F, 2.7 V capacitors in series ( $C = 108.3$  F). The initial capacitor bank voltage is 15 V. A Syren10 manufactured by Dimension Engineering is used as the servo amplifier for the capacitor bank. Control commands and sensor acquisitions are implemented with a dSPACE DS1103 PPC system that interfaces with Matlab / Simulink and ControlDesk software. The data sampling frequency is 2 kHz. The angular signal from the knee encoder is numerically differentiated and filtered with a second-order low-pass filter with a cutoff frequency of 30 Hz for input to the knee controller. The capacitor voltage is low-pass filtered with a cutoff frequency of 10 Hz. Fig. 12 illustrates the experimental setup for the 3-DOF prosthesis test robot.

The goal in this subsection is to experimentally verify that greater deviations from reference trajectories can provide better energy regeneration, and that better tracking of reference trajectories typically results in less energy regeneration. To this end, we compare a high-impedance controller with low-impedance controller, both with constant impedances. We recorded the sensor signals for 15 seconds. For both cases, we can achieve small RMS errors of 5 mm and 0.10 rad for hip displacement and

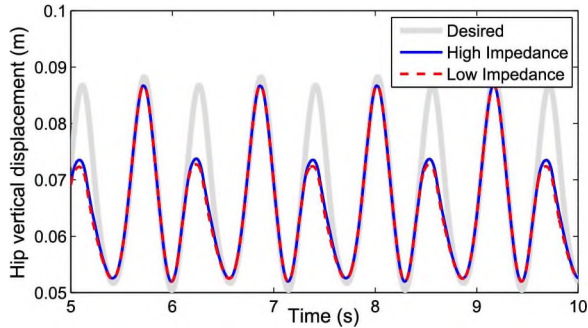


Fig. 13. Experimental results – hip joint vertical displacement with high and low constant impedance. For clarity, only five seconds are shown here.

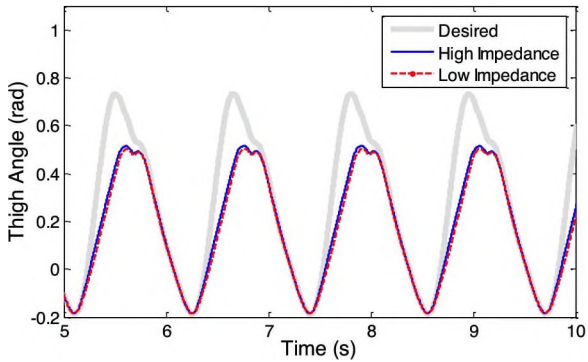


Fig. 14. Experimental results – thigh joint angle with high and low constant impedance. For clarity, only five seconds are shown here.

thigh angle, respectively. High-impedance and low-impedance control result in RMS tracking errors of 0.14 rad and 0.2 rad, respectively.

Hip displacement and thigh angle are shown in Figs. 13 and 14, respectively. These figures demonstrate worse tracking than in the simulation (compare with Fig. 4). This is due to the fact that able-bodied gait data is used as the desired trajectories for the prosthesis test robot, while: (1) the dynamics of the test robot are much different than the dynamics of human walking; (2) the lack of an ankle joint in the prosthesis influences the upper joints; and (3) the inefficiency of the servo-amplifiers for the upper joints contribute to poor tracking.

Fig. 15 illustrates the knee angle with constant impedances. In contrast to the simulation results, there is no chattering in the knee angle. This is due to the natural mechanical and electrical damping in the physical system that is not modeled in the simulation.

Fig. 16 shows the capacitor voltage change for the two different impedance settings. Linear regression is fit to the capacitor voltage to better represent the trend. The capacitor voltage of the high impedance controller has a decreasing trend while the voltage of the low impedance controller shows a slight increasing trend.

These initial experimental results verify the feasibility of prosthetic leg control with self-powered operation and even energy regeneration at the semi-active knee joint. The constant-impedance experiment provides the proof of concept,

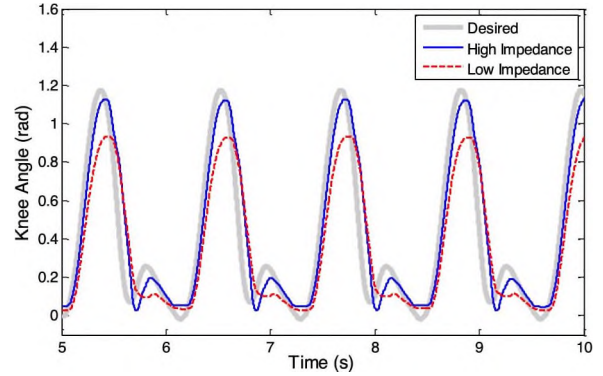


Fig. 15. Experimental results – knee joint angle with high and low constant impedance. For clarity, only five seconds are shown here.

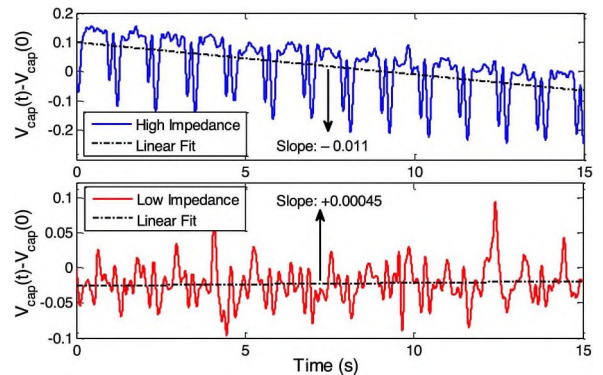


Fig. 16. Experimental results – capacitor voltage change with high and low constant impedance.

and so including results with time-varying impedance is not critical to the point of this paper. However, future work should include experimental results for time-varying impedance.

Compared with the simulation results, the experimental results demonstrate a slower energy gain with low impedance, and a faster energy loss with high impedance. That is, energy performance is worse in the experiment than in simulation. This is due to unmodeled losses and inefficiencies in the wiring, the motor, friction, and other non-ideal factors. For instance, the experiment does not control for the cable lengths, and just a few ohms can make the difference between a net charge or a net discharge, especially when we are close to the self-powered condition. It may also be due to the fact that we used a point-foot model in the simulation whereas we used a non-point foot in the experiment. However, the experimental results still demonstrate the promising potential of prosthesis control with energy regeneration.

### E. Potential Improvements and Limitations

For future work, it is of great interest to implement the controller on a prototype prosthetic leg with energy regenerative electronics for amputee use. Robust control can be implemented to account for parameter uncertainties and unusual walking scenarios in practical applications. Also, instead of using a single Pareto point for the controller, it could be possible to use a com-

combination of Pareto points to benefit from more than one solution. For instance, we could use a solution with minimum tracking error and then switch to a solution with high energy regeneration, depending on current needs and priorities. System stability during controller switching is also an important issue that will need to be carefully considered.

The limitations of this research include several factors. Although the simulations showed a net energy increase, mechanical friction was not considered in the JM model. In addition, the internal dynamics of the power converter elements and the sensors were neglected in this study. Incorporation of these factors could be an important step toward generalization and modeling accuracy. We also note that we modeled and implemented the prosthetic leg without the ankle joint. We also did not investigate the mechanism of transferring energy from the knee to the ankle joint. A general prosthetic model with both knee and ankle joints could be used in future studies to investigate the performance of the ankle joint while it is powered by the stored energy of the knee joint. This would require the design of a mechanism for power exchange between the two joints. Also, we have considered only normal walking in this paper. We will need to consider control design and energy regeneration for activities such as fast walking, stair ascent or descent, and incline walking.

## VIII. CONCLUSION

Mixed passivity based tracking/impedance control was designed for a robotic manipulator with both active and semi-active joints. Active joints were motion controlled while semi-active joints were impedance controlled. The semi-active joints are powered by a regenerative scheme that includes a JM, an energy-storing element, and a PCE. The control law for the semi-active joint is determined by an exact matching law. A desired target impedance is imposed on the relationship between external force and reference trajectory deviation. We showed that tracking accuracy and energy regeneration in the semi-active joint are competing objectives. Therefore, multi-objective optimization (MOO) was used to obtain a compromise solution.

A constrained NSBBO algorithm was used to solve the MOO problem. A prototype prosthesis test robot with 3 DOFs was used as an example. The first two DOFs are active hip displacement and thigh angle, while the third DOF is semi-active knee angle. Time-varying impedance was implemented with cubic splines, which resulted in better tracking accuracy and more stored energy than constant impedance. The simulation results indicated the feasibility of prosthetic leg control with human-like tracking performance and positive energy regeneration at the semi-active knee joint. The storage of energy in the ultracapacitor motivates the idea of transferring the surplus energy at the knee to the ankle joint. Experimental results also demonstrated energy storage at the knee joint. These results show the potential to significantly reduce power requirements in a transfemoral prosthesis. The source code used to generate these results and a video of the animated simulations are available at [54].

## ACKNOWLEDGMENT

The authors would like to thank P. Khalaf and H. E. Warner for their help with the experimental procedures.

## REFERENCES

- [1] I. Rankis *et al.*, "Utilization of regeneration energy in industrial robots system," *Power Electr. Eng., Sci. J. Riga Tech. Univ.*, vol. 31, pp. 95–100, 2013.
- [2] T. Shimizu and C. Underwood, "Super-capacitor energy storage for micro-satellites: Feasibility and potential mission applications," *Acta Astronaut.*, vol. 85, pp. 138–154, 2013.
- [3] E. Vinot and R. Trigui, "Optimal energy management of HEVs with hybrid storage system," *Energy Convers. Manage.*, vol. 76, pp. 437–452, 2013.
- [4] C. Arantes *et al.*, "Using ultracapacitors as energy-storing devices on a mobile robot platform power system for ultra-fast charging," in *Proc. Int. Conf. Inf. Contr., Autom. Robot.*, Vienna, Austria, 2014, vol. 2, pp. 156–164.
- [5] S. X. Piao *et al.*, "Development of flexible supercapacitor for mobile robot," in *Proc. 54th Annu. Conf. Soc. Instrum. Contr. Eng. Jpn.*, Hangzhou, Japan, 2015, pp. 912–915.
- [6] A. Senfelds *et al.*, "Power smoothing approach within industrial DC micro-grid with supercapacitor storage for robotic manufacturing application," in *Proc. IEEE Int. Conf. Autom. Sci. Eng.*, Gothenburg, Sweden, 2015, pp. 1333–1338.
- [7] D. B. Popovic and V. D. Kalanovic, "Output space tracking control for above-knee prosthesis," *IEEE Trans. Biomed. Eng.*, vol. 40, no. 6, pp. 549–557, Jun. 1993.
- [8] N. E. Krausz *et al.*, "Depth sensing for improved control of lower limb prostheses," *IEEE Trans. Biomed. Eng.*, vol. 62, no. 11, pp. 2576–2587, Nov. 2015.
- [9] B. Lawson *et al.*, "Control of stair ascent and descent with a powered transfemoral prosthesis," *IEEE Trans. Neural Syst. Rehabil. Eng.*, vol. 21, no. 3, pp. 466–473, May 2013.
- [10] H. Huang *et al.*, "A strategy for identifying locomotion modes using surface electromyography," *IEEE Trans. Biomed. Eng.*, vol. 56, no. 1, pp. 65–73, Jan. 2009.
- [11] K. H. Ha *et al.*, "Volitional control of a prosthetic knee using surface electromyography," *IEEE Trans. Biomed. Eng.*, vol. 58, no. 1, pp. 144–151, Jan. 2011.
- [12] B. L. Hunter, "Design of a self-contained active, regenerative, computer-controlled above-knee prosthesis," M.S. thesis, Dept. Mech. Eng., Massachusetts Inst. Technol., Cambridge, MA, USA, 1981.
- [13] B. Seth, "Energy regeneration and its application to active above-knee prostheses," Ph.D. dissertation, Dept. Mech. Eng., Massachusetts Inst. Technol., Cambridge, MA, USA, 1987.
- [14] K. A. Tabor, "The real-time digital control of a regenerative above-knee prosthesis," M.S. thesis, Dept. Mech. Eng., Massachusetts Inst. Technol., Cambridge, MA, USA, 1988.
- [15] M. Tucker and K. Fite, "Mechanical damping with electrical regeneration for a powered transfemoral prosthesis," in *Proc. IEEE/ASME Int. Conf. Adv. Intell. Mechatron.*, Montreal, QC, Canada, 2010, pp. 13–18.
- [16] A. van den Bogert *et al.*, "Modeling and optimal control of an energy storing prosthetic knee," *ASME J. Biomech. Eng.*, vol. 134, no. 5, pp. 051007-1–051007-8, 2012, doi:10.1115/1.4006680.
- [17] B. Lawson *et al.*, "Standing stability enhancement with an intelligent powered transfemoral prosthesis," *IEEE Trans. Biomed. Eng.*, vol. 58, no. 9, pp. 2617–2624, Sep. 2011.
- [18] F. Sup *et al.*, "Design and control of a powered transfemoral prosthesis," *Int. J. Robot. Res.*, vol. 27, no. 2, pp. 263–273, 2008.
- [19] T. Izumi, "Energy saving manipulator by regenerating conservative energy," in *Proc. Adv. Motion Contr. Symp.*, Nagoya, Japan, 2000, pp. 630–635.
- [20] T. Izumi *et al.*, "Optimal control of a servo system regenerating conservative energy to a condenser," in *Proc. IEEE/IAS Conf. Ind. Autom. Contr., Emerg. Technol.*, Taipei, Taiwan, 1995, pp. 651–656.
- [21] D. A. Winter, "Energy generation and absorption at the ankle and knee during fast, natural, and slow cadences," *Clin. Orthopaedics Relat. Res.*, vol. 175, pp. 147–154, 1983.
- [22] R. Unal *et al.*, "Towards a fully passive transfemoral prosthesis for normal walking," in *Proc. Int. Conf. Biomed. Robot. Biomechatron.*, 2012, pp. 1949–1954.

- [23] H. Richter *et al.*, "Semiactive virtual control method for robots with regenerative energy-storing joints," in *Proc. 19th World Congr. Int. Fed. Autom. Contr.*, Cape Town, South Africa, 2014.
- [24] H. Richter, "A framework for control of robots with energy regeneration," *ASME J. Dyn. Syst., Meas. Contr.*, vol. 137, no. 9, pp. 091004-1–091004-11, 2015, doi:10.1115/1.4030391.
- [25] D. Simon *et al.*, "Linearized biogeography-based optimization with re-initialization and local search," *Inf. Sci.*, vol. 267, pp. 140–157, 2014.
- [26] Z. Eckart *et al.*, "Comparison of multiobjective evolutionary algorithms: Empirical results," *Evol. Comput.*, vol. 8, no. 2, pp. 173–195, 2000.
- [27] G. Khademi *et al.*, "Multi-objective optimization of tracking/impedance control for a prosthetic leg with energy regeneration," in *Proc. IEEE Conf. Decis. Contr.*, Las Vegas, NV, USA, 2016, pp. 5322–5327.
- [28] G. Vael *et al.*, "The innas hydraulic transformer: The key to the hydrostatic common pressure rail," SAE Tech. Paper 2000-01-2561, 2000.
- [29] D. Karnopp *et al.*, *System Dynamics: Modeling, Simulation, and Control of Mechatronic Systems*. New York, NY, USA: Wiley, 2012.
- [30] V. Azimi *et al.*, "Stable robust adaptive impedance control of a prosthetic leg," in *Proc. ASME Dyn. Syst. Contr. Conf.*, Columbus, OH, USA, Nov. 2015, pp. 1–9, doi:10.1115/DSCC2015-9794.
- [31] M. Spong *et al.*, *Robot Modeling and Control*. New York, NY, USA: Wiley, 2006.
- [32] S. P. Chan *et al.*, "Robust impedance control of robot manipulators," *Int. J. Robot. Autom.*, vol. 6, no. 4, pp. 220–227, 1991.
- [33] H. Mohammadi and H. Richter, "Robust tracking/impedance control: Application to prosthetics," in *Proc. Amer. Contr. Conf.*, Chicago, IL, USA, 2015, pp. 2673–2678.
- [34] D. Simon, *Evolutionary Optimization Algorithms*. New York, NY, USA: Wiley, 2013.
- [35] K. Deb *et al.*, "A fast and elitist multiobjective genetic algorithm: NSGA-II," *IEEE Trans. Evol. Comput.*, vol. 6, no. 2, pp. 182–197, Apr. 2002.
- [36] S. Wright and J. Nocedal, *Numerical Optimization*. New York, NY, USA: Springer, 1999.
- [37] H. Richter *et al.*, "Dynamic modeling, parameter estimation and control of a leg prosthesis test robot," *Appl. Math. Modell.*, vol. 39, no. 2, pp. 559–573, 2014.
- [38] H. Richter and D. Simon, "Robust tracking control of a prosthesis test robot," *ASME J. Dyn. Syst., Meas. Contr.*, vol. 136, no. 3, pp. 031011–031011-12, 2014, doi:10.1115/1.4026342.
- [39] P. Khalaf and H. Richter, "Parametric optimization of stored energy in robots with regenerative drive systems," in *Proc. IEEE Int. Conf. Adv. Intell. Mechatron.*, Alberta, Canada, 2016, pp. 1424–1429.
- [40] M. Ackermann and A. J. van den Bogert, "Optimality principles for model-based prediction of human gait," *J. Biomech.*, vol. 43, no. 6, pp. 1055–1060, 2010.
- [41] G. Khademi *et al.*, "Evolutionary optimization of user intent recognition for transfemoral amputees," in *Proc. IEEE Biomed. Circuits Syst. Conf.*, Atlanta, GA, USA, Oct. 2015, pp. 1–4, doi:10.1109/BioCAS.2015.7348280.
- [42] L. Nolan *et al.*, "Adjustments in gait symmetry with walking speed in trans-femoral and trans-tibial amputees," *Gait Posture*, vol. 17, no. 2, pp. 142–151, 2003.
- [43] A. Tura *et al.*, "Gait symmetry and regularity in transfemoral amputees assessed by trunk accelerations," *J. Neuroeng. Rehabil.*, vol. 7, no. 1, pp. 1–10, 2010, doi:10.1186/1743-0003-7-4.
- [44] B. E. Lawson *et al.*, "A robotic leg prosthesis: Design, control, and implementation," *IEEE Robot. Autom. Mag.*, vol. 21, no. 4, pp. 70–81, Dec. 2014.
- [45] I. C. Trelea, "The particle swarm optimization algorithm: Convergence analysis and parameter selection," *Inf. Process. Lett.*, vol. 85, no. 6, pp. 317–325, 2003.
- [46] N. B. Reese and W. D. Bandy, *Joint Range of Motion and Muscle Length Testing*. Amsterdam, The Netherlands: Elsevier, 2013.
- [47] K. M. Ostrosky *et al.*, "A comparison of gait characteristics in young and old subjects," *Phys. Ther.*, vol. 74, no. 7, pp. 637–644, 1994.
- [48] P. C. Rowe *et al.*, "Impaired range of motion of limbs and spine in chronic fatigue syndrome," *J. Pediatrics*, vol. 165, no. 2, pp. 360–366, 2014.
- [49] P. Khalaf *et al.*, "Multi-objective optimization of impedance parameters in a prosthesis test robot," in *Proc. ASME Dyn. Syst. Contr. Conf.*, Columbus, OH, USA, Oct. 2015, pp. 1–9, doi:10.1115/DSCC2015-9848.
- [50] D. A. Winter, "Kinematic and kinetic patterns in human gait: Variability and compensating effects," *Hum. Mov. Sci.*, vol. 3, nos. 1/2, pp. 51–76, 1984.
- [51] D. A. Winter, *Biomechanics and Motor Control of Human Movement*. New York, NY, USA: Wiley, 2009.
- [52] A. J. van den Bogert *et al.*, "A real-time system for biomechanical analysis of human movement and muscle function," *Med. Biol. Eng. Comput.*, vol. 51, no. 10, pp. 1069–1077, 2013.
- [53] H. Mohammadi *et al.*, "Multi-objective optimization of decision trees for power system voltage security assessment," in *Proc. IEEE Syst. Conf.*, Orlando, FL, USA, 2016, pp. 1–6, doi:10.1109/SYSCON.2016.7490524.
- [54] G. Khademi. (2016, Dec. 23). Energy Regeneration MATLAB® Source Code. [Online]. Available: <http://embeddedlab.csuohio.edu/prosthetics/energy-regeneration.html>